

Sand transverse dune aerodynamics: 3D coherent flow structures from a computational study

*Original*

Sand transverse dune aerodynamics: 3D coherent flow structures from a computational study / Bruno, L., Fransos, D.. -  
In: JOURNAL OF WIND ENGINEERING AND INDUSTRIAL AERODYNAMICS. - ISSN 0167-6105. - STAMPA. -  
147:(2015), pp. 291-301. [10.1016/j.jweia.2015.07.014]

*Availability:*

This version is available at: 11583/2649999 since: 2016-09-19T15:52:09Z

*Publisher:*

Elsevier

*Published*

DOI:10.1016/j.jweia.2015.07.014

*Terms of use:*

This article is made available under terms and conditions as specified in the corresponding bibliographic description in the repository

*Publisher copyright*

(Article begins on next page)

## **Highlights**

- Sand dune aerodynamics investigated within a computational study
- Simulation of different experimental setup
- Comparison between computational results and experimental measurements
- Emerging 3D coherent, mushroom-like flow structures in a nominally 2D setup
- Some good practices in dune aerodynamics are recommended

# Sand transverse dune aerodynamics: 3D Coherent Flow Structures from a computational study

Luca Bruno<sup>a,c,\*</sup>, Davide Fransos<sup>b,c</sup>

<sup>a</sup>*Politecnico di Torino, Department of Architecture and Design,  
Viale Mattioli 39, I-10125, Torino, Italy*

<sup>b</sup>*Optiflow Company,*

*160, Chemin de la Madrague-Ville, F-13015, Marseille, France*

<sup>c</sup>*Windblown Sand Modeling and Mitigation joint research group*

---

## Abstract

The engineering interest about dune fields is dictated by their interaction with a number of human infrastructures in arid environments. Sand dunes dynamics is dictated by wind and its ability to induce sand erosion, transport and deposition. A deep understanding of dune aerodynamics serves then to ground effective strategies for the protection of human infrastructures from sand, the so-called sand mitigation. Because of their simple geometry and their frequent occurrence in desert area, transverse sand dunes are usually adopted in literature as a benchmark to investigate dune aerodynamics by means of both computational or experimental approaches, usually in nominally 2D setups. The present study aims at evaluating 3D flow features in the wake of a idealised transverse dune, if any, under different nominally 2D setup conditions by means of computational simulations and to compare the obtained results with experimental measurements available in literature.

*Keywords:* dune aerodynamics, Computational Wind Engineering, 3D flow, mushroom-like coherent flow structures

---

\*Corresponding author. Tel: (+39) 011.090.4870. Fax: (+39) 011.090.4999.

Email address: [luca.bruno@polito.it](mailto:luca.bruno@polito.it) (Luca Bruno)

URL: <http://www.polito.it/wsmm> (Luca Bruno)

## 1. Introduction

The engineering interest about dune fields is dictated by their interaction with a number of human infrastructures in arid environments, such as roads and railways, pipelines, industrial facilities, farms, buildings (e.g. [Alghamdi and Al-Kahtani, 2005](#)). Some of such undesired effects are shown in Figure 1. The

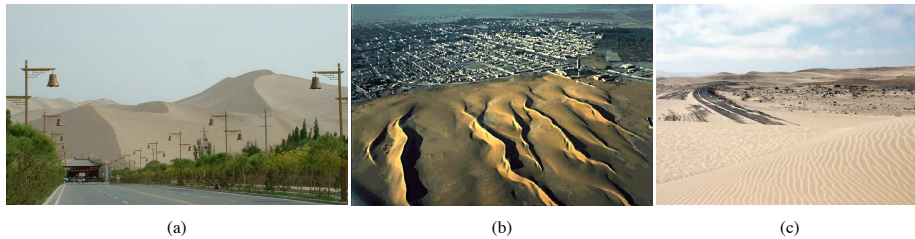


Figure 1: Windblown sand interaction with anthropic activities: megadunes surrounding a road and farmlands in Dunhuang, Gansu Province, PRC. Photo: I.A. Inman, 2007 (a), linear dunes encroaching Nouakchott, capital of Mauritania. Landsat 1565-10032-6, 1974 (b), loose sand covering the Aus to Lüderitz railway line, Namibia. Photo: K. Dierks, 2003 (c)

development, shape and migration of dunes depend fundamentally on availability of mobile sediment, on the incoming wind directionality, and on the flow structures of local disturbed wind ("topographically forced wind" in Geomorphology literature), that is on the wind ability to induce sand erosion, transport and deposition. In particular, coherent flow structures embedded within fluid flow fields are considered to govern the magnitude, form and scaling of sediment transport events ([Bauer et al., 2013](#)), and the dune shape in turn. Hence, a wind-focused perspective has been adopted in aeolian dune geomorphology in order to investigate the former to explain the latter. In wind engineering, a deep understanding of dune aerodynamics serves to ground effective strategies for the protection of human infrastructures from sand, the so-called sand mitigation. In areas of constant wind direction and under high sand availability, the transverse dune - which has nearly fixed profile in the direction perpendicular to the wind - is the prevailing dune type ([Livingstone and Warren, 1996](#)). Furthermore, ideal sharp-crested transverse dune, i.e. without crest-brink separation ([Bauer](#)

21 [et al., 2013](#)), are usually adopted in fundamental aerodynamic studies for their  
 22 geometric simplicity. Previous studies (e.g. [Lancaster, 1995](#)) have revealed that  
 23 transverse dunes generally have upwind (windward, stoss) slope angles ranging  
 24 between  $2^\circ \leq \alpha_u \leq 20^\circ$  and downwind (leeward) slope angles ranging between  
 25  $28^\circ \leq \alpha_d \leq 34^\circ$ , i.e. around the sand friction static angle. For sake of clarity, a  
 26 simplified 2D scheme of the transverse dune geometry and of the flow around it  
 is given in Figure 2. The aerodynamic behaviour of sand dunes in atmospheric

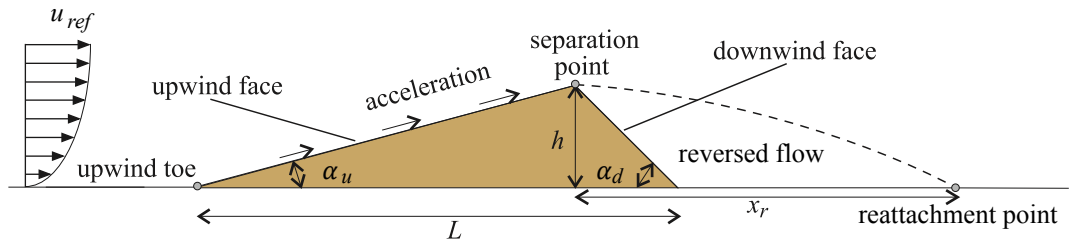


Figure 2: Ideal sharp crest, transverse dune aerodynamics scheme

27  
 28 boundary layer belongs to the very general class of bluff bodies and to the general  
 29 one of hills (for a review, see e.g. [Bitsuamlak et al., 2004](#)). The incoming  
 30 wind flow is first fairly decelerated at the upwind toe, then strongly accelerated  
 31 along the dune upwind face straight up to crest. The separation of the boundary  
 32 layer then occurs at the crest itself. The naturally inclined downwind face is  
 33 surrounded by a reversed flow region, whose extent is one of the key parameters  
 34 describing the flow. Reattachment of the boundary layer occurs far downstream  
 35 the dune crest, being  $x_r$  the so-called reattachment length. The latter quantity  
 36 is experienced in sharp-edge bluff body aerodynamics to be highly sensitive to  
 37 a number of setup parameters (e.g. Reynolds number, surface roughness, in-  
 38 coming turbulence). Much more detailed 2D topological mapping of the wake  
 39 region for isolated transverse dunes under crest-normal flow can be recovered  
 40 in literature (e.g. [Walker and Nickling, 2002, 2003](#); [Delgado-Fernandez et al.,](#)  
 41 [2011](#)).

42 While the 2D flow structures above have been extensively scrutinized and re-

43 viewed in [Livingstone et al. \(2007\)](#), very little is known about three-dimensional  
44 coherent flow structures in the wake (for an updated review, see [Bauer et al.,](#)  
45 [2013](#)). On one hand, in the Geomorphology community, such 3D coherent flow  
46 structures past nominally 2D dunes are usually ascribed to: i. oblique incom-  
47 ing wind, i.e. where a yaw angle  $\alpha_C > 45^\circ$  gives rise to helical vortices in the  
48 wake ([Allen, 1970](#); [Walker and Nickling, 2002](#)), and/or ii. small crest irregu-  
49 larities, inducing spanwise flow in the wake, spanwise swirling of the reversed  
50 flow, and secondary recirculation zones (see the recent CFD simulations and  
51 field measurements in [Jackson et al., 2011, 2013](#); [Delgado-Fernandez et al.,](#)  
52 [2013](#), , respectively). It is worth pointing out that from an aerodynamic point  
53 of view both occurrences involve a 3D setup. On the other hand, to the writers  
54 best knowledge, 3D coherent structures in the wake of genuine 2D setups (i.e.  
55 ideal transverse dune under normal wind) remain elusive and scarcely studied  
56 in literature, if any. Difficulties in both wind tunnel facilities and measurement  
57 techniques, and in 3D computational simulations are conjectured by the writers  
58 and other authors (e.g. [Walker and Nickling, 2003](#)) to be the cause of such lack  
59 of knowledge.

60 On one side, Wind Tunnel (WT) tests in the aeolian field adopt scaled dune mod-  
61 els spanning across the whole test section width (i.e.  $S = w$ ), and with rather  
62 low values of the dune aspect ratio (span/chord ratio  $S/L$ ), e.g.  $S/L = 1.28$  in  
63 [Walker \(2000\)](#) and [Walker and Nickling \(2003\)](#),  $1.92 \leq S/L \leq 10.32$  in [Dong](#)  
64 [et al. \(2007\)](#); [Qian et al. \(2009\)](#),  $S/L = 5.4$  in [Liu et al. \(2011\)](#)). Such values of  
65 the aspect ratios:

- 66 • are by far lower than the ones adopted in other bluff body aerodynamics  
67 problems characterised by separation, reversed flow and reattachment,  
68 especially when 3D flow features are expected (see for instance [Bruno](#)  
69 [et al., 2014](#));
- 70 • are suspected to significantly affect the 3D features of the flow in the wake,  
71 because of the tips effects due to interaction between the boundary layers  
72 surrounding the dune and the WT side walls. For instance, in [Walker and](#)

73 [Nickling \(2003, Figure 5a, page 1119\)](#) the normalised shear stress profile  
74 along the WT midline (i.e. .46 m far from the WT side wall) does not  
75 reach nil value in the conjectured reattachment area nor elsewhere in the  
76 dune wake.

77 More generally, difficulties in WT studies are recognised in the proper scaling of  
78 different setup lengths, i.e. the ones related to the dune geometry, the surface  
79 roughness, the turbulent length scale of the turbulent incoming flow ([Walker  
80 and Nickling, 2003](#)).

81 On the other side, the fundamental computational (CFD) studies on the flow  
82 field over the transverse dune (e.g. [Parsons et al., 2004a,b](#); [Schatz and Herrmann,  
83 2006](#); [Araújo et al., 2013](#)) usually consider simplified 2D condition (see [Living-  
84 stone et al., 2007](#), for a review). Only recently, [Liu et al. \(2011\)](#) have compared  
85 the simulated flow around a transverse dune obtained in 2D and "2.5D" condi-  
86 tions between them and with WT measurements. The "2.5D" heading indicates  
87 that despite the computational domain is 3D, its height and width are equal to  
88 half the WT working section dimensions where reference experimental test are  
89 performed. In other terms, both left-to-right and bottom-to-top symmetry of  
90 the flow are conjectured to reduce the domain size and related computational  
91 costs. Under such an assumption, interesting preliminary results are obtained.  
92 In particular, 3D flow features of the flow in the near wake of the 2D dune are  
93 qualitatively observed ([Liu et al., 2011, Figure 8a, page 884](#)). According to the  
94 writers, some questions immediately follow. Which aerodynamic phenomena  
95 underly and/or trigger the 3D flow features observed in the cited experiments  
96 and computational simulations? In particular, do the WT side wall effects play  
97 any role in generating such 3D structures? That is, would similar structures  
98 having corresponding characteristic lengths obtain if the same dune had, in the  
99 limit, an infinitely long span (i.e., an infinite aspect ratio)?

100 The present study aims at shedding some light on such issues. The sensitiv-  
101 ity of the 3D features of the wake to the setup geometrical scaling is studied. In  
102 particular, the domain size and the related inlet and side boundary conditions

103 are the retained parameters of the study. In such a perspective, the present  
104 study takes the baton relay from the stimulating study of (Liu et al., 2011)  
105 conceived in the Geomorphology community, and develops it according to the  
106 knowledge background of Bluff Body Aerodynamics. The adopted computa-  
107 tional approach is expected to efficiently complement the wind tunnel studies in  
108 exploring a huge number of setup conditions, where a single parameter is varied  
109 at the time and border, or even unphysical, conditions can be scrutinized. The  
110 experimental setup of Liu et al. (2011) is adopted as the reference one. The  
111 obtained computational results are compared with the experimental ones avail-  
112 able in literature. Finally, a deeper insight in the 3D emerging coherent flow  
113 structures in the wake is provided.

## 114 2. Wind flow modelling and computational approach

115 The incompressible, turbulent, separated, unsteady flow around the dune  
116 profile is modeled by the classical Time-dependent Reynolds Averaged Navier-  
117 Stokes (T-RANS) equations, which, in Cartesian coordinates, read:

$$\frac{\partial \bar{u}_i}{\partial x_i} = 0 \quad (1)$$

$$\frac{\partial \bar{u}_i}{\partial t} + \bar{u}_j \frac{\partial \bar{u}_i}{\partial x_j} = -\frac{1}{\rho} \frac{\partial \bar{p}}{\partial x_i} + \frac{\partial}{\partial x_j} \left[ \nu \left( \frac{\partial \bar{u}_i}{\partial x_j} + \frac{\partial \bar{u}_j}{\partial x_i} \right) \right] - \frac{\partial}{\partial x_j} (\overline{u'_i u'_j}), \quad (2)$$

119 where  $\bar{u}_i$  is the averaged velocity,  $u'$  the velocity fluctuating component,  $\bar{p}$  the  
120 averaged pressure,  $\rho$  the air density and  $\nu$  the air kinematic viscosity. The SST  
121  $k - \omega$  turbulence model first proposed by Menter (1994) and further modified  
122 in Menter et al. (2003) is used to close the T-RANS equations:

$$\frac{\partial k}{\partial t} + \bar{u}_i \frac{\partial k}{\partial x_i} = \frac{\partial}{\partial x_i} \left[ (\sigma_k \nu_t + \nu) \frac{\partial k}{\partial x_i} \right] + \tilde{P}_k - \beta^* k \omega \quad (3)$$

$$\frac{\partial \omega}{\partial t} + \bar{u}_i \frac{\partial \omega}{\partial x_i} = \frac{\partial}{\partial x_i} \left[ (\sigma_\omega \nu_t + \nu) \frac{\partial \omega}{\partial x_i} \right] + \alpha \frac{\omega}{k} P_k - \beta \omega^2 + (1 - F_1) \frac{2\sigma_\omega}{\omega} \frac{\partial k}{\partial x_i} \frac{\partial \omega}{\partial x_i}, \quad (4)$$

124 where  $k$  is the turbulent kinetic energy,  $\omega$  its specific dissipation rate and  $\nu_t$   
125 the so-called turbulent kinematic viscosity. The kinetic energy production term

126  $\tilde{P}_k$  is modeled by introducing a production limiter to prevent the build-up of  
 127 turbulence in stagnation regions:

$$\tilde{P}_k = \min(P_k, 10\beta^*k\omega) \quad \text{being} \quad P_k \approx 2\nu_t D_{ij} \frac{\partial \bar{u}_i}{\partial x_j}.$$

128 For sake of conciseness, the definition of the blending function  $F_1$  and the values  
 129 of the model constants are omitted herein. Interested readers can find them in  
 130 [Menter et al. \(2003\)](#). The SST  $k - \omega$  turbulence model is selected for the  
 131 current application because of its proven accuracy in bluff body aerodynamics  
 132 in general ([Menter et al., 2003](#)) and in dune aerodynamics in particular ([Liu](#)  
 133 [et al., 2011](#)).

134 At the ground and dune surfaces the so-called sand-grain roughness wall func-  
 135 tions are selected for the current application because of their wide use in environ-  
 136 mental CWE in general (e.g. [Blocken et al., 2007a](#)) and the proofs of adequacy  
 137 obtained in previous 3D simulations of sand dune aerodynamics by [Liu et al.](#)  
 138 [\(2011\)](#); [Jackson et al. \(2011, 2013\)](#). In particular, standard wall functions ([Lau-](#)  
 139 [nder and Spalding, 1974](#)) with roughness modification ([Cebeci and Bradshaw,](#)  
 140 [1977](#)) are applied. The equivalent sand grain roughness height is determined  
 141 as  $K_s = 9.793z_0/C_s$ , where  $C_s = 0.5$  is the roughness constant and  $z_0$  is the  
 142 aerodynamic roughness. All the application setups involve  $z_0 = 0.1$  mm and  
 143 shear velocity  $u^* = 0.512$  m/s, both estimated in wind tunnel tests. It follows  
 144  $K_s = 1.96$  mm, and non-dimensional roughness height  $K_s^+ = K_s u^* / \nu \approx 70$ , in  
 145 the so-called transitional regime [Blocken et al. \(2007a\)](#).

146 The adopted computational domains and the conditions imposed at their  
 147 boundaries are the object of a parametrical study. They are detailed in the  
 148 next Section.

149 The OpenFoam©Finite Volume open source code is used in the following to  
 150 numerically evaluate the flow-field. The cell-centre values of the variables are  
 151 interpolated at face locations using the second-order Central Difference Scheme  
 152 for the diffusive terms. The convection terms are discretised by means of the  
 153 so-called Limited Linear scheme, a 2nd order accurate bounded Total Varia-  
 154 tional Diminishing (TVD) scheme resulting from the application of the Sweby

155 limiter (Sweby, 1984) to the central differencing in order to enforce a mono-  
 156 tonicity criterion. The pressure-velocity coupling is achieved by means of the  
 157 pressure-implicit PISO algorithm, using a predictor-corrector approach for the  
 158 time discretisation of the momentum equation, whilst enforcing the continuity  
 159 equation. The space discretization is accomplished by a predominantly struc-  
 160 tured grid of hexahedral control volumes. Unstructured patterns locally occur  
 161 at the intersection between the surface-fitted grid boundary layer and the carte-  
 162 sian grid in the higher part of the domain. The denser grid is located close  
 163 to the wind tunnel floor and side walls, and to the dune surface. The grid in  
 164 the whole domain and its detail around the dune surface are shown in Figure  
 3(a) and (b), respectively. The height of the control volume adjacent to the

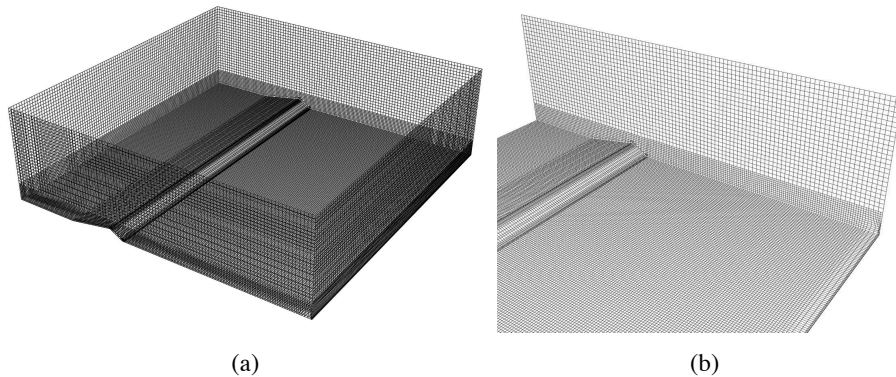


Figure 3: Computational grid in the whole domain (a) and close to the dune (b)

165  
 166 wall  $n_w = 2n_p$  is driven by the sand-grain roughness wall function requirements  
 167 (Blocken et al., 2007b). In particular,  $n_w$  should i. provide a sufficiently high  
 168 mesh resolution in the normal direction  $n$  to the surface, ii. comply with the  
 169 standard requirement on dimensionless wall unit  $30 < n^+ = n_p u^* / \nu < 100$ , and  
 170 iii. be longer than twice the sand grain roughness height,  $K_s = 1.96$  mm in  
 171 the considered setup. The third requirement obeys to the need of avoiding grid  
 172 cells with centre points within the physical roughness height. Both the second  
 173 and third requirements limit the grid density at wall. In the following,  $n_w$  is

174 set equal to  $n_w = 0.2h = 5$  mm in order to satisfy at best the above criteria.  
 175 The  $n^+$  value along the flat surface far upwind and downwind from the dune  
 176 is  $n^+ = 80$ , while its values along the dune surface vary from  $n^+ = 70$  and  
 177  $n^+ = 35$  at the dune upwind and downwind toes, respectively, to  $n^+ = 110$  at  
 178 the dune crest. The ratio  $n_p/K_S = 1.28$  is larger but close to unit: hence no  
 179 significant further grid refinement at wall can be done within the adopted wall  
 180 treatment. The advancement in time is accomplished by the implicit two-step  
 181 second order Backward Differentiation Formulae (BDF) method. The adopted  
 182 time step is equal to  $\Delta t = 0.00025$  [s], i.e.  $\Delta t u_{ref}/h = 0.1$  dimensionless time  
 183 unit.

### 184 3. Application setup

185 Three setups are adopted and the resulting flow are compared. All of them  
 186 adopt a sharp-crested transverse dune, and generally refer to the experimen-  
 187 tal setup described by [Liu et al. \(2011\)](#). Besides such main reference, critical  
 188 comparison is also made to other measurements provided in [Dong et al. \(2007\)](#);  
 189 [Qian et al. \(2009\)](#); [Walker and Nickling \(2003\)](#), the former two being obtained  
 190 for several incoming speeds, the latter in slightly different experimental condi-  
 191 tions. Table 1 summarizes the main features of the cited experimental setups,  
 192 where  $z_0$  is the dune and floor aerodynamic roughness and  $u_{ref}$  is the incom-  
 193 ing reference speed. It follows that the reference Reynolds number is equal to  
 194  $Re_h = u_{ref}h/\nu = 1.7e + 4$ .

195 The setups differ in both the size of the analytical domain in space and in the  
 196 corresponding applied boundary conditions (b.c.). The domain size and the  
 197 kind of b.c. adopted in the setups are depicted in Figure 4, while the profiles of  
 198 the incoming wind (mean velocity  $u_x$ , turbulence intensity  $It$  and length scale  
 199  $Lt$ ) are plotted in Figure 5. The setups are briefly commented in the following:

200 **s1** only 1/4 of the wind tunnel working section volume is retained. Symmetry  
 201 conditions are imposed on the vertical plane because of the conjectured  
 202 symmetry of the flow. Free stream b.c.s are set on the upper horizontal

Table 1: Experimental setups

Authors	$h$ [mm]	$\alpha_u$ [deg]	$\alpha_d$ [deg]	$L/h$ [-]	$S/L$ [-]	$u_{ref}$ [m/s]	$z_0$ [mm]
Liu et al. (2011)						10	
Dong et al. (2007)	25	10	30	7.4	5.40	8,10,12,14	0.1
Qian et al. (2009)						8,10,12,14	
Walker and Nickling (2003)	80	8	30	9.0	1.28	8,13,18	n.a.

203 plane to disregard the influence of the WT upper wall. The incoming  
204 mean wind velocity and turbulence intensity profiles are fitted on the  
205 WT measurements (Liu et al., 2011, estimated shear velocity  $u^* = 0.512$   
206 m/s), while turbulence length scale is conjectured constant and equal to  
207  $Lt = 5$  mm because of the lack of experimental data (Figure 5). The  
208 spatial grid involves about  $4.e + 5$  control volumes. This setup is often  
209 retained in CFD practice to reduce the number of grid volumes and related  
210 computational costs when the WT conditions are to be emulated (e.g. in  
211 Liu et al., 2011). The setup is intended to discuss the accuracy of such an  
212 approach;

213 **s2** the setup exactly reproduces the size of the WT working section in Dong  
214 et al. (2007); Qian et al. (2009); Liu et al. (2011). No-slip b.c.s are set  
215 at the four alongwind boundary planes to model the WT walls. A com-  
216plementary simulation (s2-a, Figure 4) is preliminary performed along an  
217empty channel to replicate the WT approaching section described in Liu  
218et al. (2011). Periodic conditions at the inlet and outlet of s2-a are set to  
219obtain a fully self-developed, horizontally homogeneous incoming bound-  
220ary layer flow (Blocken et al., 2007b). The resulting  $u_x$ ,  $It$  and  $Lt$  profiles  
221are then imposed at the inlet of the main domain (Figure 5). The spatial  
222grid in s2-b involves about  $1.5e + 6$  control volumes. The setup aims

223 at removing the ansatz introduced in s1 in order to suggest best practice  
 224 guidelines in CFD simulations of WT tests;

225 **s3** The side walls of the WT working section are replaced by spanwise periodic  
 226 conditions. Two domain spanwise lengths are considered:  $w_{3a} = w_2$  is set  
 227 in setup s3a, and  $w_{3a} = 4w_2$  in setup s3b. The height of the domain  
 228 is set equal to  $12h$ , i.e. larger than the range suggested in [Franke et al.](#)  
 229 [\(2007\)](#)  $4h < h_{WT} < 10h$  for external flows in Wind Engineering. The  
 230 spatial grid in s3b involves about  $2.7e + 6$  control volumes. The setup  
 231 aims at comparing the results to the ones obtained in the s2 setup and  
 232 at evaluating 3D flow features, if any, under 2D, "external" incoming  
 233 flow conditions. The profiles of the incoming turbulent length scale and  
 234 turbulence intensity are set in accordance to [Richards and Norris \(2011\)](#)  
 235 to replicate an external flow.

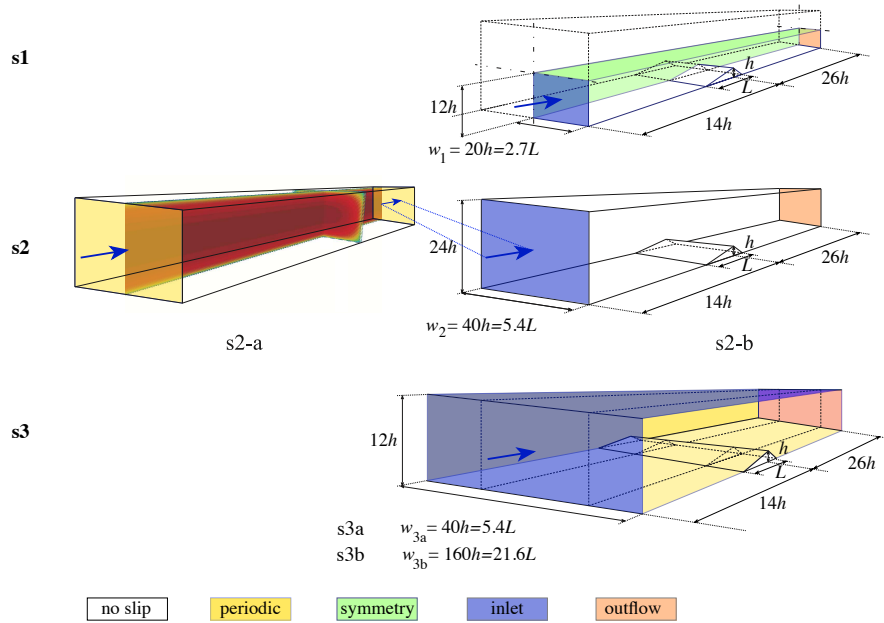


Figure 4: Scheme of the adopted setup conditions (not in scale) including b.c. (wind from left to right)

236 In all setups, Neumann conditions ("outflow" in Figure 4) involving the velocity  
 237 field and the pressure (null normal component of the stress tensor) as well as  $k$   
 238 and  $\omega$  are imposed at the outlet boundary. No-slip conditions are imposed at the  
 floor surface and at the WT walls, if any. Uniform initial conditions are imposed

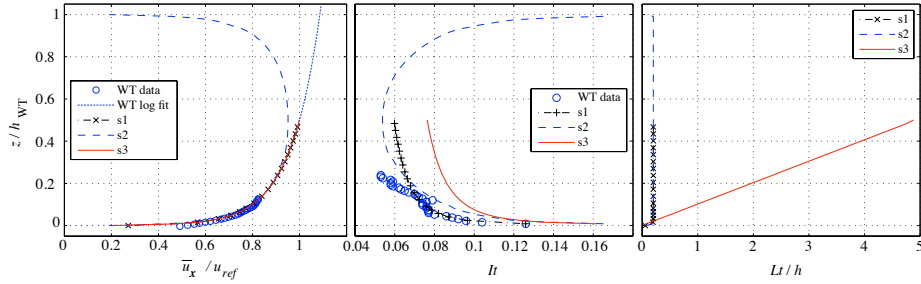


Figure 5: Vertical profiles of the inlet boundary conditions

239  
 240 at the beginning of the time-dependent simulations. The simulated time for each  
 241 setup is equal to about  $Tu_{ref}/h = 4000$  dimensionless time units, long enough  
 242 to guarantee the convergence of the first and second statistical moments in time  
 243 for all the flow variable, following the convergence check proposed by [Bruno](#)  
 244 [et al. \(2010\)](#). The simulations have been performed thanks to the Optiflow  
 245 pc cluster (32 nodes with 4 cores each, 4 Gb RAM per node, Intel Nehalem  
 246 2.8 GHz clock, 1.4 Tflops). An overall cpu time of about 25 hours on 63 cores  
 247 results for the complete parametrical study.

## 248 4. Results

### 249 4.1. Setup effects on the overall flow regime

250 In this section, the time dependent behavior of the simulated flow in the  
 251 three setups is discussed with reference to both bulk and local quantities. The  
 252 former is defined as the aerodynamic coefficient  $C_D(t)$  of drag force per span-  
 253 wise unit length that results from integration of the stress field on the dune  
 254 downwind face, Figure 6(a). The Power Spectral Density of the drag coefficient  
 255 is plotted versus the dimensionless frequency  $f^* = fh/u_{ref}$  in Figure 6(b).

The PSDs in both s1 and s2 setups clearly show a well defined peak at about

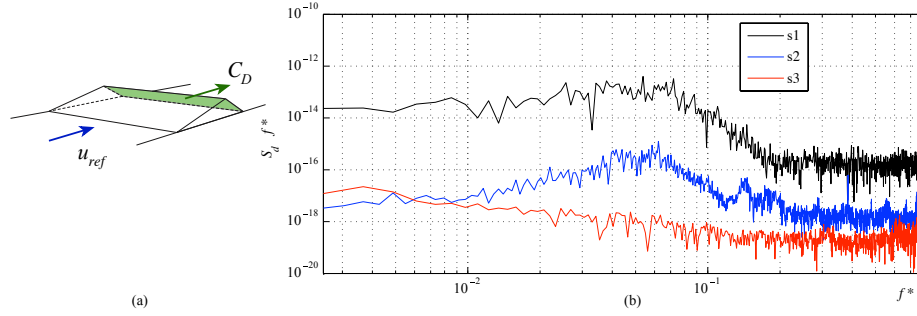


Figure 6: Time dependent flow: PSD of the drag coefficient

256

257  $f^* \approx 0.05 = St$ , that conversely disappears in s3a and s3b setups (both notated  
 258 "s3" in the following, if not specified otherwise, for the sake of simplicity). At  
 259 such Strouhal number  $St$  the power density in setup s1 is one order of magni-  
 260 tude higher than the one in s2, that is in turn by far greater than in s3. The  
 261 high frequency fluctuations ( $f^* > 3e - 1$ ) are due to spurious numerical oscil-  
 262 lations of the solution. In summary, the drag force resulting from s3 is almost  
 263 steady ( $std(C_D) \approx 5.6e - 7$ ), while very weak to moderate time fluctuations in  
 264 the remaining setups ( $std(C_D) \approx 7.3e - 5$  and  $std(C_D) \approx 1.e - 3$  in s2 and  
 s1, respectively ) suggest a localized unsteadiness of the flow. To prove such

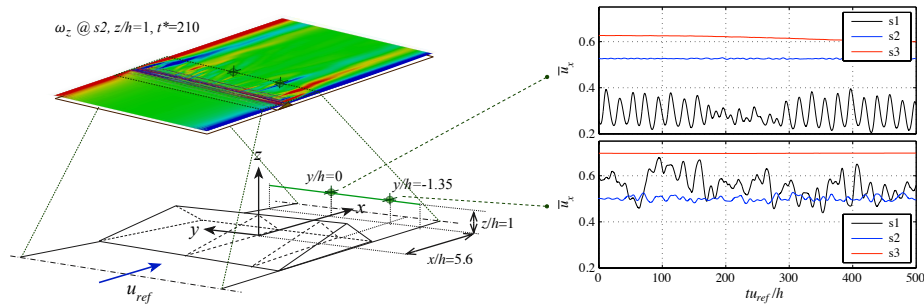


Figure 7: Time dependent flow: spanwise position of the time dependent phenomena

265

266 conjecture, the time history of the longitudinal component of the velocity  $u_x$

267 is plotted for the three setups and at two probes in the wake (Figure 7). In  
 268 s1 and s2, the closer the probe to the WT side wall, the larger the velocity  
 269 fluctuations, while in s3 the flow in the wake is almost steady everywhere. An  
 270 instantaneous field of the  $z$ -vorticity on the plane  $z/h = 1$  for s2 is provided in  
 271 the same Figure to shed some light on the underlying fluid flow phenomenon.  
 272 In fact, the interaction between the separated boundary layer at the dune crest  
 273 and the attached one along the WT sidewall induces a 3D flapping along the  
 274 latter.

275 As previously introduced, the reattachment length  $x_r$  is one of the most relevant  
 276 quantities in transverse dune aerodynamics. In the adopted computational ap-  
 277 proach, the reattachment point is evaluated as the one in which the longitudinal  
 278 component  $\tau_x$  of the shear stress change sign downwind the dune downwind toe.  
 279 Heaving in mind the weak variability in time of the overall flow, the time aver-  
 280 aged reattachment point ( $t - avg(x_r)$ ) is evaluated, while its spanwise trend is  
 281 described by the reattachment line, i.e.  $t - avg(x_r(y))$ . The latter ones obtained  
 282 in the three setups are plotted in Figure 8.

283 The following remarks follow:

- 284 • very significant WT wall effects take place close to the dune tips in both  
 285 s1 and s2 setups. In particular:
  - 286 - in s1 such effects propagate along all the dune span, so that a mean-  
 287 ingful estimate of the reattachment length can be obtained by span-  
 288 wise averaging nor by adopting a point wise value, e.g. at the mid  
 289 plane;
  - 290 - in s2 the spanwise variability due to the WT side wall is limited  
 291 to a distance from the wall of about  $d \approx 1.5L$ , clearly related to  
 292 the unsteady plumes pointed out in Figure 7. A central segment  
 293 with nearly constant  $x_r$  can be recognized: at the vertical mid plan  
 294 ( $y = 0$ )  $x_r \approx 6.35h$ , pretty close to the value measured by [Dong et al.](#)  
 295 ([2007](#)) ( $x_r \approx 6h$ ) in the same setup conditions;
- 296 • unexpectedly, a quasi-periodic, "festoon-shaped" spanwise reattachment

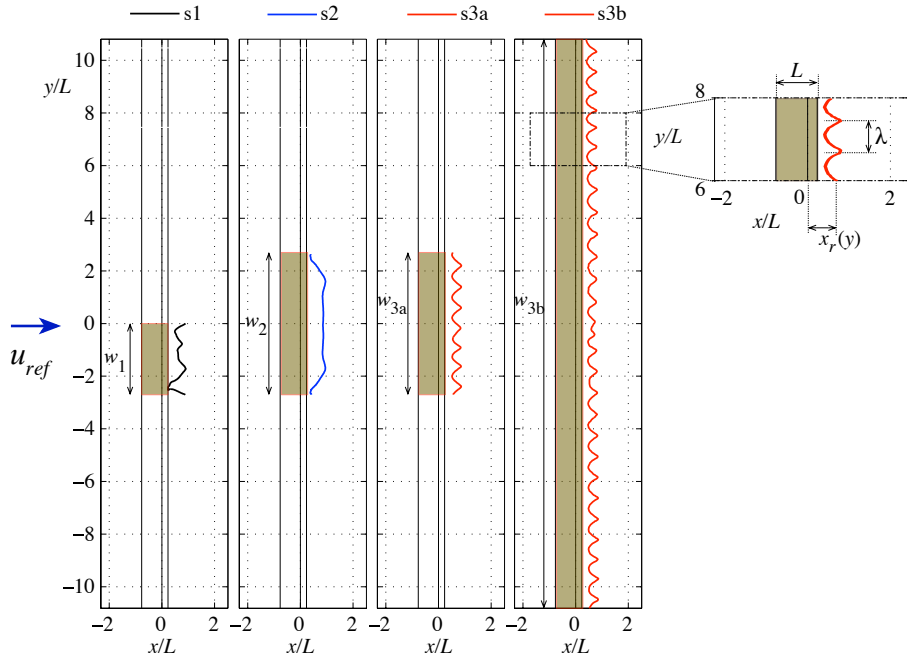


Figure 8: Spanwise dependent flow: variation of the reattachment line

297 line emerges from both simulations s3a and s3b. Such a trend allows to  
 298 estimate some spanwise statistics.

299 - The first two statistical moments of the reattachment length, i.e. its  
 300 mean value  $y - avg(t - avg(x_r))$  and standard deviation  $y - std(t -$   
 301  $avg(x_r))$ , are:

302 **s3a**  $y - avg(t - avg(x_r)) = 5.04h$ ,  $y - std(t - avg(x_r)) = 0.82h$ ;

303 **s3b**  $y - avg(t - avg(x_r)) = 4.64h$ ,  $y - std(t - avg(x_r)) = 0.88h$ .

304 It is worth pointing out that in both simulations the mean value  
 305  $y - avg(t - avg(x_r))$  is significantly lower than the one obtained at  
 306 the mid-plan in s2.

307 - Let us define a characteristic spanwise length (or wavelength)  $\lambda$  of  
 308 the reattachment line (see closeup view in Figure 8). Its spanwise  
 309 statistics are:

310 **s3a**  $y - avg(t - avg(\lambda)) = 5.61h$ ,  $y - std(t - avg(\lambda)) = 0.43h$ ;

311 **s3b**  $y - avg(t - avg(\lambda)) = 5.75h$ ,  $y - std(t - avg(\lambda)) = 0.36h$ .

312 The value of the standard deviation  $y - std(t - avg(\lambda))$  is small in  
313 both simulations, that is the festoon shape is quite stable spanwise.

314 - Finally it is worth pointing out that the spanwise dimension  $w_{3a}$  in  
315 setup s3a accommodates 7 wavelengths (including the two halves at  
316 the domain side), while the one  $w_{s3b} = 4w_{s3a}$  in setup s3b accommo-  
317 dates 27 waves plus an oscillation at midspan, i.e. at the far section  
318 from the lateral periodic b.c.s.

319 In summary, the findings obtained in the Section prove significant effects of the  
320 WT side walls (s1 and s2) on the overall flow regime, and suggest that they  
321 inhibit the triggering of an almost periodic spanwise variability of the flow in  
322 the wake, as observed in external flow conditions (s3).

#### 323 4.2. Comparison between WT measurements and CWE results

324 In this Section, comparisons between time-averaged WT measurements at  
325 the dune midspan ( $y/L = 0$ ) and the present computational results obtained in  
326 the different setups are provided. Bearing in mind the quasi-periodic spanwise  
327 reattachment line in s3 (Fig. 8), also spanwise statistics are evaluated for such  
328 setup. The  $z$ -wise profiles of the longitudinal component of the velocity  $u_x$  have  
329 been measured in WT tests by Liu et al. (2011) using PIV at different positions  
330 in the the vertical mid plan ( $y = 0$ ) of the WT working section. These profiles  
331 are compared to the computational ones in Figure 9. The scatter with the WT  
332 data around the upwind face (Figure 9, lines a-b) are probably due, according  
333 to Liu et al. (2011), to the limitation of the PIV system, which cannot fully  
334 resolve the high-speed gradient in the near-surface zone and leads to nonzero  
335 wind speed at the surface. The agreement in the reversed flow region (Figure  
336 9, lines e-f) is excellent for setup s2, that replicates the WT conditions. The  
337 computational results from setup s1 strongly overestimate the speed deficit in  
338 the near wake, while the  $y - avg(t - avg(\bar{u}_x))$  in s3 is quite different form the

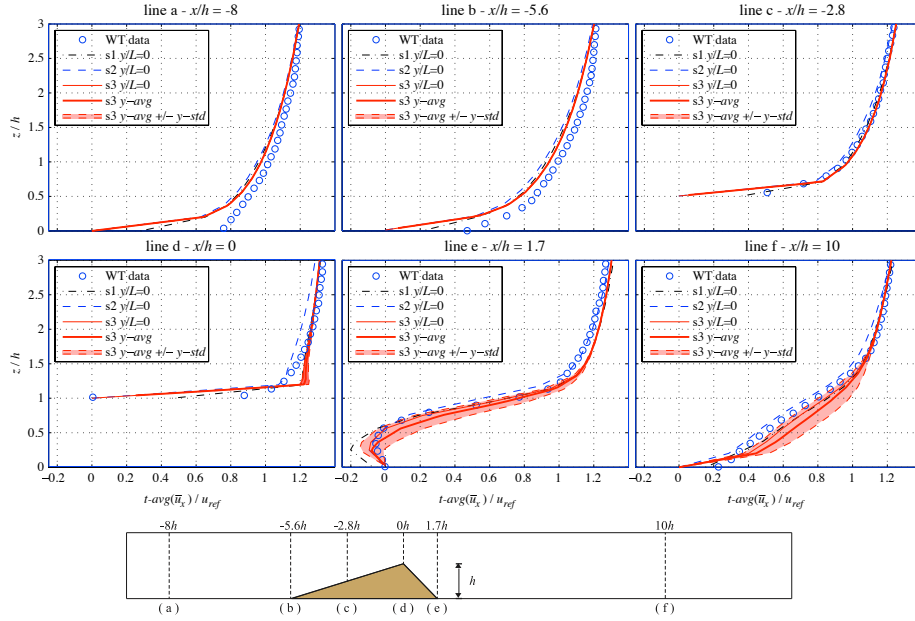


Figure 9: Horizontal velocity profiles: WT measurements (Liu et al., 2011) and present CWE results

339 centre plane one and from WT data. In the same setup, a significant spanwise  
 340 deviation occurs in the wake (Figure 9, lines e-f).

341 The measured  $x$ -wise profiles of the vertical component of the velocity  $u_y$  at  
 342 the level  $z \approx h$  are reported in Qian et al. (2009). PIV technique has been  
 343 adopted on the WT vertical mid plan ( $y = 0$ , i.e. at a distance from the side  
 344 wall  $d/L = 2.7$ ) at different reference velocities of the incoming wind. The  $u_y$   
 345 profiles obtained in the three computational setups are compared among them  
 346 in Figure 10(a), while the profiles measured at midspan are compared in Figure  
 347 10(b) to the computational ones at different distance from the side wall in setup  
 348 s2. Considerable differences between s1 and s2 can be observed in the far wake  
 349 only, while a dramatic change in the vertical component of the velocity occurs in  
 350 s3 especially in the near wake. At the dune downwind face ( $0 < x/h < 1.7h$ ),  $u_y$   
 351 changes its sign from positive (upward flow, s1 and s2) to negative (downward  
 352 flow, s3). In other terms, the 2D clockwise recirculating region which character-

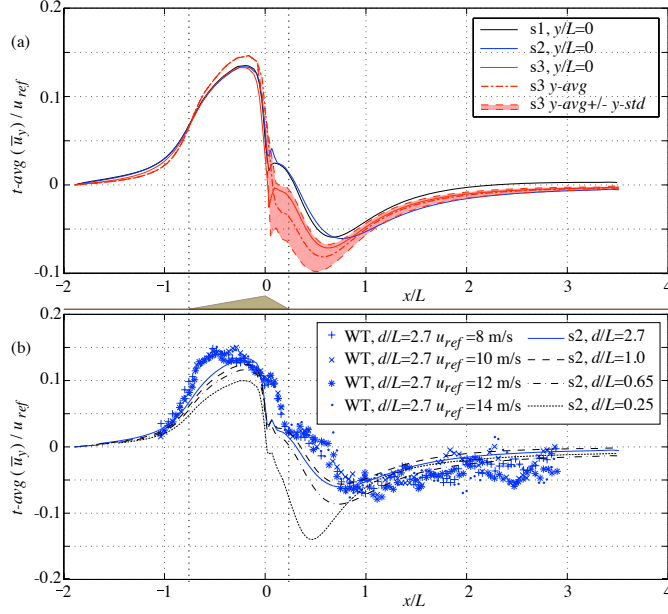


Figure 10: Vertical velocity profiles: WT measurements (Qian et al., 2009) and present CWE results

353 izes the near wake topology in s2 at mid line no longer holds and it is suspected  
 354 to change in a 3D local flow (see the large spanwise standard deviation of  $u_y$ ). A  
 355 satisfactory agreement is observed between WT and computational approaches,  
 356 if the same setup and distance from the side wall is adopted (blue points and  
 357 continuous line in Fig. 10-b). Conversely, the closer the vertical plan to the  
 358 side wall, the smaller the upward speed at the upwind face and the higher the  
 359 downward speed at the downwind surface.

360 An analogous post processing is proposed for the  $x$ -wise profiles of the shear  
 361 stress magnitude  $|\tau|$  at the floor in Figure 11. The shear stress is a quantity of  
 362 particular interest in windblown sand dynamics because above a given threshold  
 363 value  $\tau_t$  it induces the sand grain saltation, i.e. the sand bed erosion. Conversely,  
 364 at  $|\tau| < \tau_t$  sedimentation of the flying grains occurs (Bagnold, 1941). For such  
 365 reason, the  $|\tau|/\tau_t$  obtained by computations in the three setups is plotted in  
 366 Figure 11(a). s1 fails in predicting the sedimentation just downwind the crest

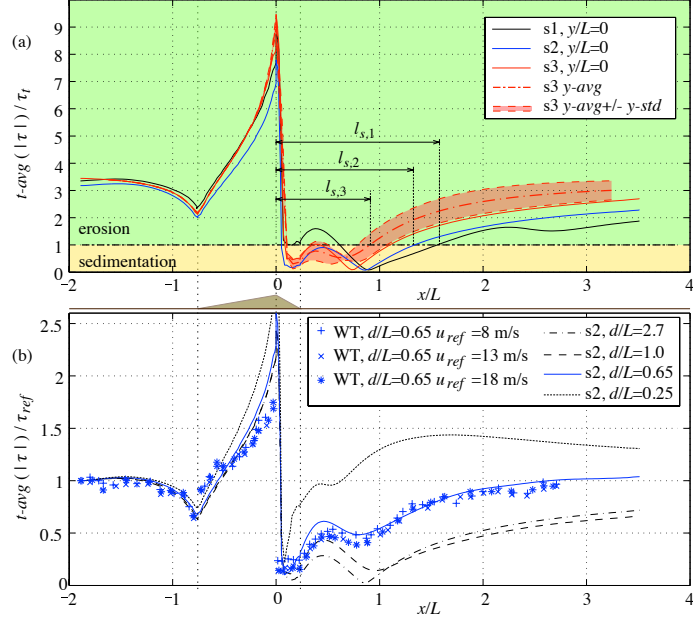


Figure 11: Shear stress profiles: Wind Tunnel measurements (Walker and Nickling, 2003) and present CWE results

367 and the downwind toe. The lower the blockage ratio, the shorter the sedimen-  
 368 tation length  $l_s$ , i.e. the closer to the dune the point from which erosion takes  
 369 place again. Once more, the spanwise variability of the profile along the wake is  
 370 significant in s3, and the sedimentation length varies from about  $0.75L$  to  $1.1L$ .  
 371 Figure 11(b) compares the shear stress magnitude profiles obtained in s2 with  
 372 the one measured by Walker and Nickling (2003) in their WT test by using  
 373 Irwin-type differential pressure sensors. It is worth pointing out that in this  
 374 case the experimental setup differs from the computational one in the dune  
 375 cross section, in the dune aspect ratio, and in the Reynolds number (see Table  
 376 1). On one hand, the smaller angle of the upwind face  $\alpha_u$  in WT test induces  
 377 the lower shear stress magnitude along it. On the other hand, the  $|\tau|$  profile  
 378 downwind the crest is mainly affected by the dune aspect ratio, i.e. by the  
 379 distance  $d$  of the measurement alignment from the WT side wall. In fact, a  
 380 very good agreement is obtained when the measurements at the WT mid plan

381 (i.e.  $d = 0.5S/L \approx 0.65$ ) are compared to the computational profile at the same  
 382 distance from the side wall. The closer the alignment to the side wall, the higher  
 383  $|\tau|$  along the wake. In other terms, in this case study the WT wall side effects  
 384 are by far larger than the ones induced by  $L/h$  and/or  $u_{ref}$ , even if much more  
 385 emphasis is traditionally given to the latter than to the former.

### 386 4.3. 3D Coherent Flow Structures

387 This final Section aims at providing a sound phenomenological reading of the  
 388 spanwise variability in simulated in external flow conditions (setup s3). A deeper  
 389 insight in the flow characteristics is then performed, thanks to the amount of in-  
 390 formation available from computational simulations. Advanced post-processing  
 391 and flow visualization techniques are employed to this aim. In particular, the  
 392 velocity and shear stress vector fields are visualized on selected planes by us-  
 393 ing the so-called Line Integral Convolution (LIC, Cabral and Leedom, 1993;  
 394 Stalling and Hege, 1995; Laramée et al., 2003). Some information are provided  
 395 herein, being a technique scarcely used in the Wind Engineering field.

396 LIC is based upon locally filtering an input texture along a curved stream line  
 397 segment in a vector field and it is able to depict directional information at high  
 398 spatial resolutions. The directional structure of a vector field can be graphically  
 399 depicted by its stream lines, i.e. paths whose tangent vectors coincide with  
 400 the vector field. Given a pixel  $\mathbf{x}_0$  of the desired resulting image and numeri-  
 401 cally computed a streamline  $\sigma$ , passing by  $\mathbf{x}_0 = \sigma(s_0)$ , line integral convolution  
 402 consists in calculating the intensity for that pixel as

$$I(\mathbf{x}_0) = \int_{s_0-L}^{s_0+L} k(s-s_0)T(\sigma(s))ds, \quad (5)$$

403 where  $s$  is the arc-length coordinate,  $T$  is an input texture,  $2L$  is the filter length  
 404 and  $k$  is a filter kernel normalized to unity. In LIC visualizations of fluid flows,  
 405 a white noise or similar random image is chosen as input texture  $T$ . The con-  
 406 volution causes pixel intensities to be highly correlated along individual stream  
 407 lines, but independent in directions perpendicular to them. In the resulting  
 408 images the directional structure of the vector field is clearly visible.

409 Figure 12(a) and (b) show the LIC visualization of the time-averaged velocity  
 410 field on an ideal inclined plane ( $\beta = 12^\circ$ ) crossing the near wake from the dune  
 411 crest, and the LIC visualization of the time-averaged shear stress field on the  
 412 dune downwind face and wake floor, respectively. In both figures, the direction  
 of the field is highlighted by superimposed arrowed lines. The most striking

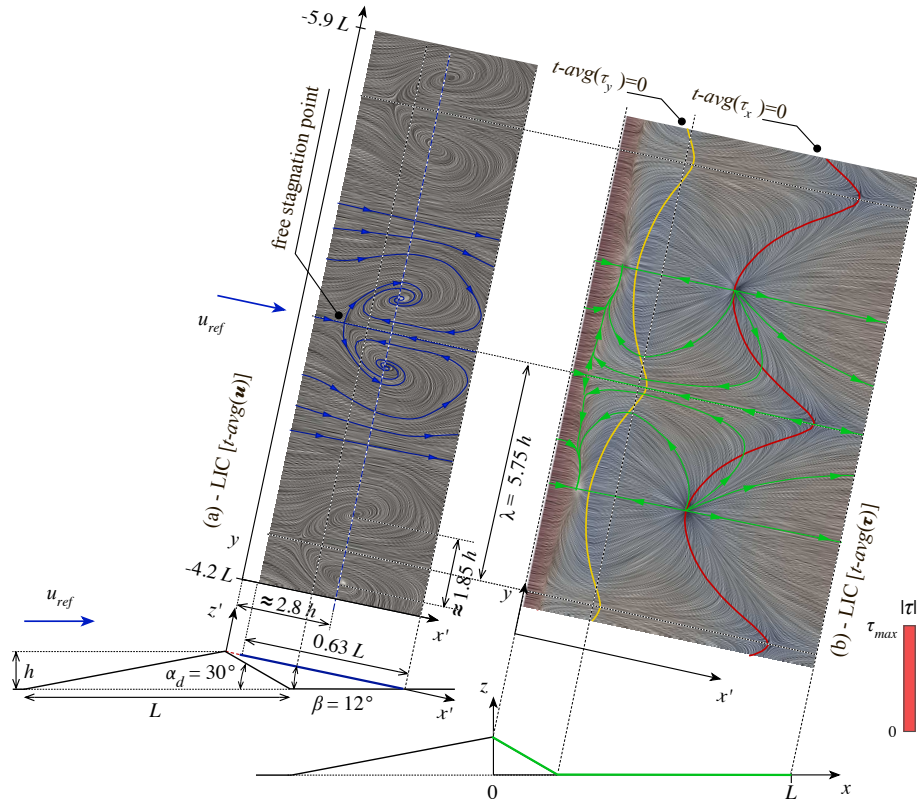


Figure 12: Spanwise 3D coherent structures in the dune wake: time averaged velocity field (a), time averaged shear stress field colored by the its modulus (b)

413  
 414 result is that in Figure 12(a), where the LIC of the time-averaged velocity field  
 415 highlights quasi-steady, "mushroom"-like coherent flow structures having a pair  
 416 of owl eyes each. These structures consists of two counterrotating foci with a  
 417 free stagnation point downwind the crest and between the foci. The main di-  
 418 mensions of such structures are given in the figure. The corresponding LIC of

419 time-averaged shear stress field (Fig. 12-b) is even more complicated and char-  
 420 acterized by a "skein"-like pattern. The pattern shape appears to be strongly  
 421 related with the mushroom-like structure, especially at the ground floor (i.e.  
 422 where the mushroom is closest to the floor). In order to shed some more light  
 423 in such a pattern, it is colored by the modulus of the same shear stress, and  
 424 the spanwise lines along which  $\tau_y = 0$  and  $\tau_x = 0$  (reattachment line, see also  
 425 Fig. 8) are superimposed. For both lines a geometrical reading with respect to  
 426 the LIC pattern can be provided: the former is the locus of points where the  
 427 tangent to the streamlines are aligned with the  $x$ -axis, while the latter is the  
 428 locus of points where the tangent to the streamlines are aligned with the  $y$ -axis.  
 429 The mushroom spanwise characteristic length is equal to the wavelength  $\lambda$  of  
 430 the "festoon" reattachment line. In particular, the spanwise maximum reat-  
 431 tachment length correspond to the mushroom center, while the minimum value  
 432 takes place in between two consecutive mushrooms.  
 433 To the authors' best knowledge, analogous spanwise coherent flow structures  
 434 have been previously recognized at least in two studies involving nominally 2D  
 435 setups.  
 436 Similar spanwise mushroom-shaped flow structures have been visualized by  
 437 [Schewe \(2001\)](#) around an apparently different aerodynamic setup, i.e. the sep-  
 438 arated flow around an airfoil at incidence in the critical regime. In fact, in  
 439 his pioneering and seminal work Schewe has observed and described in detail  
 440 mushroom-like flow structures (Figure 13), combined in different arrangements  
 441 for different values of the airfoil aspect ratio  $S/L$  ( $L = w$ ), and bounded by dis-  
 442 turbed regions close to the end plates. On the basis of the experimental results,  
 443 Schewe conjectures that: i. the occurrence and number of the mushroom-like  
 444 structures depend on the inclination of the base upper surface; ii. the spanwise  
 445 flow structure remains intact as  $S/L \rightarrow \infty$ ; iii. the wavelength  $\lambda$  scales with the  
 446 sectional dimension(s) of the airfoil; iv. preferential or more natural spanwise  
 447 arrangements exist, in terms of number of cells and their wavelength. These  
 448 speculations seem to hold, to a certain extent, also in the present case study.  
 449 In fact: i. the downwind face of the dune and the base upper surface of the

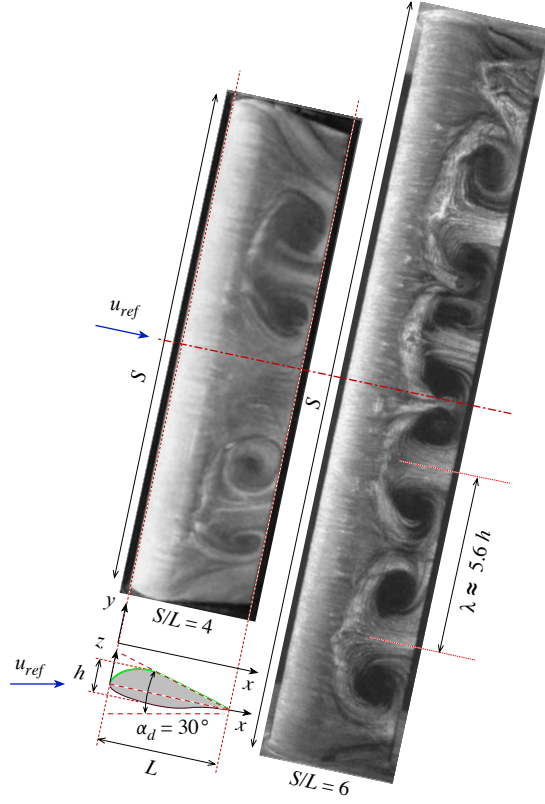


Figure 13: Oil-flow pictures of the mushroom-like flow structures at the upper surface of an airfoil, after [Schewe \(2001\)](#)

450 airfoil share the same inclination with respect to the incoming wind ( $\alpha_d \approx 30^\circ$ );  
 451 ii. setup s3 confirms that the coherent flow structure is qualitatively unchanged  
 452 by passing from s3a to s3b, where the latter mimics an infinite aspect ratio of  
 453 the dune because of the periodic side b.c. and the increased spanwise length;  
 454 iii. the characteristic length  $\lambda$  of the mushrooms found by [Schewe \(2001\)](#) is  
 455 comparable to the one in s3, if both are scaled versus  $h$  ( $\lambda \approx 5.75h$ , Fig. 12-a,  
 456  $\lambda \approx 5.6h$ , Fig. 13); iv. in both Schewe and present setups, stable arrangements  
 457 are characterized by a given number of spanwise aligned mushrooms. In Schewe,  
 458 an even number of vortices is always observed, but the end-plate disturbances  
 459 considerably extend spanwise; conversely, in s3 an odd number of mushrooms

460 emerges in both s3a (7) and s3b (27) setups (see Fig. 8), despite the spanwise  
461 length in s3b is four time the one in s3a. It is worth pointing out that the  
462 quasi-periodic mushroom structure is corrupted at midspan, if the dune length  
463  $S = w$  is not an odd multiple of  $\lambda$  (s3b). Despite the analogies above, it is  
464 worth pointing out that the flow structures in Schewe (2001) are recognized only  
465 in the critical regime, while the occurrence of the same condition is unlikely in  
466 the present case study.

467 More recently, analogous 3D, global, quasi-steady vortices have been simulated  
468 by Spalart et al. (2014) in an even more different fluid flow setup, i.e. the nom-  
469 inally 2D, high Reynolds number, fully developed turbulent Couette flow. The  
470 RANS-based simulations of Spalart et al. (2014) (including the SST  $k - \omega$  one),  
471 successfully reproduce the same flow structures previously observed and sim-  
472 ulated in experiments and DNS, respectively. In the present perspective, it is  
473 worth pointing out that: i. the vortices are arranged in a quasi-periodic z-wise  
474 system of counter-rotating pairs (Fig. 1, Spalart et al. (2014)), analogously to  
475 the arrangement in Figure 12(a) ; ii. the distribution of the skin-friction coef-  
476 ficient in the  $z$  direction (Fig. 6, Spalart et al. (2014)) qualitatively matches  
477 the "festoon-shaped" spanwise reattachment line in Figure 8; iii. the simulated  
478 flow structures hold in a wide range of Reynolds numbers, and the effect of the  
479 vortices is only weakly dependent on Re. In their outlook, Spalart et al remark  
480 that there is a convincing scale separation between the simulated flow structures  
481 and the turbulence which is represented by the RANS model. The vortices have  
482 a lateral scale much smaller than the scale of the geometry (which is infinite in  
483 the setup), and random locations in  $z$ , giving them the nature of an instability.  
484 The remarks above qualitatively hold also in the present case study. Despite  
485 such analogies, it is worth pointing out that the flow structures in Spalart et al.  
486 (2014) are somewhat triggered by an initial velocity field mimicking a periodic  
487 system of counter-rotating vortex pairs in the  $(y - z)$  plane, while in the present  
488 case study the mushroom-like structures spontaneously develop from uniform  
489 initial conditions.

490

## 491 5. Conclusions

492 The present study points out some emerging 3D coherent flow structures  
493 in the wake of a transverse dune under different setup conditions by means of  
494 computational simulations and compares the obtained results with a number of  
495 experimental wind tunnel measurements available in literature. The comparison  
496 shows a good and robust agreement of the CWE results to WT data, and it goes  
497 beyond: it puts in evidence common misunderstandings in setting up computa-  
498 tional and experimental models for CWE/WT validation. Some good practices  
499 in dune aerodynamics CWE simulations and WT tests are recommended: i.  
500 CWE-WT comparisons require the careful simulation of the WT setup, includ-  
501 ing the wind tunnel geometry; ii. forcing the flow symmetry by b.c. in CWE  
502 can strongly affect the results; iii. high values aspect ratio are recommended in  
503 WT test to replicate external flow conditions, e.g.  $w/L \gg 10$ .

504 Surprisingly, emerging mushroom-like, coherent flow structures in the dune wake  
505 are clearly shown by a deep analysis of the CWE results. They are compared  
506 to analogous flow structures arising from rather different aerodynamic setups  
507 belonging to referential literature in fluid dynamics. It follows that the studied  
508 setup can be ascribed to a wider class of 3D flows occurring under 2D nominal  
509 conditions. According to the authors such class of flow seems to be of high  
510 relevance in modern developments of fluid dynamics, and it still remain poorly  
511 understood in its general features, if any. The authors hope further indepen-  
512 dent studies will appear and further develop their contribution. In particular,  
513 the precise definition of the aerodynamic regime(s) at which mushrooms grow in  
514 the dune near wake remain an open issue. An even wider computational study  
515 would be required to discuss the permanence and/or changes of such coherent  
516 flow structures form the model scale to the full scale, e.g. by varying Reynolds  
517 number and/or surface roughness.

518 **Acknowledgments**

519 The study has been developed in the framework of the Windblown Sand  
520 Modeling and Mitigation joint research, development and consulting group es-  
521 tablished between Politecnico di Torino and Optiflow Company. The authors  
522 wish to thank Luigi Preziosi and Nicolas Coste, members of the WSMM group,  
523 for the helpful discussions about the topics of the paper. Günter Schewe is grate-  
524 fully acknowledged for his kind availability in providing his flow visualizations  
525 and for his stimulating remarks.

526 **References**

- 527 Alghamdi, A.A., Al-Kahtani, N.S., 2005. Sand Control Measures and Sand  
528 Drift Fences. *J. Perform. Constr. Facil.* 19, 295–299. doi:[10.1061/\(ASCE\)](https://doi.org/10.1061/(ASCE)0887-3828(2005)19:4(295))  
529 [0887-3828\(2005\)19:4\(295\)](https://doi.org/10.1061/(ASCE)0887-3828(2005)19:4(295)).
- 530 Allen, J.R.L., 1970. *Physical processes of sedimentation*. George Allen and  
531 Unwin Ltd.
- 532 Araújo, A.D., Parteli, E.J.R., Pöschel, T., Andrade, J.S., Herrmann, H.J., 2013.  
533 Numerical modeling of the wind flow over a transverse dune. *Nature Sci. Rep.*  
534 3. doi:[10.1038/srep02858](https://doi.org/10.1038/srep02858).
- 535 Bagnold, R., 1941. *The Physics of Blown Sand and Desert Dunes*. Methuen.
- 536 Bauer, B.O., Walker, I.J., Baas, A.C.W., Jackson, D.W.T., Neuman, C.M.,  
537 Wiggs, G.F.S., Hesp, P.A., 2013. Critical Reflections on the Coherent Flow  
538 Structures Paradigm in Aeolian Geomorphology, in: *Coherent Flow Struc-*  
539 *tures at Earths Surface*. John Wiley & Sons, Ltd, pp. 111–134. doi:[10.1002/](https://doi.org/10.1002/9781118527221.ch8)  
540 [9781118527221.ch8](https://doi.org/10.1002/9781118527221.ch8).
- 541 Bitsuamlak, G., Stathopoulos, T., Bedard, C., 2004. Numerical evaluation of  
542 wind flow over complex terrain: review. *Journal of Aerospace Engineering*  
543 17, 135–145. doi:[10.1061/\(ASCE\)0893-1321\(2004\)17:4\(135\)](https://doi.org/10.1061/(ASCE)0893-1321(2004)17:4(135)).

- 544 Blocken, B., Carmeliet, J., Stathopoulos, T., 2007a. Cfd evaluation of wind  
545 speed conditions in passages between parallel buildings - effect of wall-function  
546 roughness modifications for the atmospheric boundary layer flow. *Journal of*  
547 *Wind Engineering and Industrial Aerodynamics* 95, 941–962.
- 548 Blocken, B., Stathopoulos, T., Carmeliet, J., 2007b. CFD simulation of the  
549 atmospheric boundary layer: wall function problems. *Atmos. Environ.* 41,  
550 238–252. doi:[10.1016/j.atmosenv.2006.08.019](https://doi.org/10.1016/j.atmosenv.2006.08.019).
- 551 Bruno, L., Fransos, D., Coste, N., Bosco, A., 2010. 3d flow around a rectangular  
552 cylinder: A computational study. *Journal of Wind Engineering and Industrial*  
553 *Aerodynamics* 98, 263–276.
- 554 Bruno, L., Salvetti, M., Ricciardelli, F., 2014. Benchmark on the aerodynamics  
555 of a rectangular 5:1 cylinder: An overview after the first four years of activity.  
556 *Journal of Wind Engineering and Industrial Aerodynamics* 126, 87–106.
- 557 Cabral, B., Leedom, L.C., 1993. Imaging vector fields using line integral con-  
558 volution, in: *SIGGRAPH '93*, ACM Press, New York, New York, USA. pp.  
559 263–270. doi:[10.1145/166117.166151](https://doi.org/10.1145/166117.166151).
- 560 Cebeci, T., Bradshaw, P., 1977. *Momentum transfer in boundary layers*. Wash  
561 DC Hemisphere Publ Corp N Y McGraw-Hill Book Co.
- 562 Delgado-Fernandez, I., Jackson, D.W.T., Cooper, J.A.G., Baas, A.C.W., Bey-  
563 ers, J.H.M., Lynch, K., 2013. Field characterization of three-dimensional  
564 lee-side airflow patterns under offshore winds at a beach-dune system. *J.*  
565 *Geophys. Res.-Earth* 118, 706–721. doi:[10.1002/jgrf.20036](https://doi.org/10.1002/jgrf.20036).
- 566 Delgado-Fernandez, I., Jackson, D.W.T., Cooper, J.A.G., Baas, A.C.W., Lynch,  
567 K., Beyers, J.H.M., 2011. Re-attachment zone characterisation under offshore  
568 winds blowing over complex foredune topography. *Journal of Coastal Research*  
569 64, 273–277.

- 570 Dong, Z., Qian, G., Luo, W., Wang, H., 2007. A wind tunnel simulation of  
571 the effects of stoss slope on the lee airflow pattern over a two-dimensional  
572 transverse dune. *J. Geophys. Res.* 112. doi:[10.1029/2006JF000686](https://doi.org/10.1029/2006JF000686).
- 573 Franke, J., Hellsten, A., Schlunzen, H., Carissimo, B., 2007. Best practice  
574 guideline for the CFD simulation of flows in the urban environment. COST  
575 Action 732, Quality Assurance and Improvement of Microscale Meteorological  
576 Models.
- 577 Jackson, D.W.T., Beyers, J.H.M., Delgado-Fernandez, I., Baas, A.C.W.,  
578 Cooper, J.A.G., Lynch, K., 2013. Airflow reversal and alternating corkscrew  
579 vortices in foredune wake zones during perpendicular and oblique offshore  
580 winds. *Geomorphology* 187, 86–93.
- 581 Jackson, D.W.T., Beyers, J.H.M., Lynch, K., Cooper, J.A.G., Baas, A.C.W.,  
582 Delgado-Fernandez, I., 2011. Investigation of three-dimensional wind flow  
583 behaviour over coastal dune morphology under offshore winds using com-  
584 putational fluid dynamics (cfd) and ultrasonic anemometry. *Earth Surface  
585 Processes and Landforms* 36, 1113–1124.
- 586 Lancaster, N., 1995. *Lancaster: Geomorphology of Desert Sand Dunes*. Rout-  
587 ledge, Cambridge, England.
- 588 Laramee, R.S., Jobard, B., Hauser, H., 2003. Image space based visualization  
589 of unsteady flow on surfaces, in: *VIS '03*, IEEE, Washington, DC, USA. pp.  
590 131–138. doi:[10.1109/visual.2003.1250364](https://doi.org/10.1109/visual.2003.1250364).
- 591 Launder, B.E., Spalding, D.B., 1974. The numerical computation of turbulent  
592 flows. *Comput. Methods. Appl. Mech. Eng.* 3, 269–289.
- 593 Liu, B., Qu, J., Zhang, W., Qian, G., 2011. Numerical simulation of wind flow  
594 over transverse and pyramid dunes. *J. Wind Eng. Ind. Aerod.* 99, 879–888.  
595 doi:[10.1016/j.jweia.2011.06.007](https://doi.org/10.1016/j.jweia.2011.06.007).
- 596 Livingstone, I., Warren, A., 1996. *Aeolian Geomorphology: an introduction*.  
597 Longman, London, England.

- 598 Livingstone, I., Wiggs, G.F.S., Weaver, C.M., 2007. Geomorphology of desert  
599 sand dunes: A review of recent progress. *Earth-Sci. Rev.* 80, 239–257. doi:[10.1016/j.earscirev.2006.09.004](https://doi.org/10.1016/j.earscirev.2006.09.004).  
600
- 601 Menter, F.R., 1994. Two-equation eddy-viscosity turbulence models for engi-  
602 neering applications. *AIAA Journal* 32, 269–289. doi:[10.2514/3.12149](https://doi.org/10.2514/3.12149).
- 603 Menter, F.R., Kuntz, M., Langtry, R., 2003. Ten years of industrial experience  
604 with the SST turbulence model, in: Hanjalić, K., Nagano, Y., Tummers, J.  
605 (Eds.), *Turbulence Heat and Mass Transfer 4: Proceedings of the Fourth*  
606 *International Symposium on Turbulence, Heat and Mass Transfer*, Antalya,  
607 Turkey, 12-17 October, 2003, Begell House. p. 1208.
- 608 Parsons, D.R., Walker, I.J., Wiggs, G.F.S., 2004a. Numerical modelling of  
609 flow structures over idealized transverse aeolian dunes of varying geometry.  
610 *Geomorphology* 59, 149–164. doi:[10.1016/j.geomorph.2003.09.012](https://doi.org/10.1016/j.geomorph.2003.09.012).
- 611 Parsons, D.R., Wiggs, G.F.S., Walker, I.J., Ferguson, R.I., Garvey, B.G., 2004b.  
612 Numerical modelling of airflow over an idealised transverse dune. *Environ.*  
613 *Modell. & Softw.* 19, 153–162. doi:[10.1016/S1364-8152\(03\)00117-8](https://doi.org/10.1016/S1364-8152(03)00117-8).
- 614 Qian, Dong, Luo, Wang, 2009. Variations of horizontal and vertical velocities  
615 over two-dimensional transverse dunes: A wind tunnel simulation of the effect  
616 of windward slope. *J. Arid Environ.* 73, 8–8. doi:[10.1016/j.jaridenv.2009.](https://doi.org/10.1016/j.jaridenv.2009.06.006)  
617 [06.006](https://doi.org/10.1016/j.jaridenv.2009.06.006).
- 618 Richards, P., Norris, S., 2011. Appropriate boundary conditions for computa-  
619 tional wind engineering models revisited. *Journal of Wind Engineering and*  
620 *Industrial Aerodynamics* 99, 257–266.
- 621 Schatz, V., Herrmann, H.J., 2006. Flow separation in the lee side of transverse  
622 dunes: A numerical investigation. *Geomorphology* 81, 207–216. doi:[10.1016/](https://doi.org/10.1016/j.geomorph.2006.04.009)  
623 [j.geomorph.2006.04.009](https://doi.org/10.1016/j.geomorph.2006.04.009).

- 624 Schewe, G., 2001. Reynolds-number effects in flow around more-or-less bluff bod-  
625 ies. *J. Wind Eng. Ind. Aerod.* 89, 1267–1289. doi:[10.1016/S0167-6105\(01\)](https://doi.org/10.1016/S0167-6105(01)00158-1)  
626 [00158-1](https://doi.org/10.1016/S0167-6105(01)00158-1).
- 627 Spalart, P., Garbaruk, A., Strelets, M., 2014. Rans solutions in couette flow  
628 with streamwise vortices. *International Journal of Heat and Fluid Flow* 49,  
629 128–134.
- 630 Stalling, D., Hege, H.C., 1995. Fast and resolution independent line integral  
631 convolution, in: *Proceedings of the 22nd annual conference on Computer*  
632 *graphics and interactive techniques - SIGGRAPH '95*, ACM Press, New York,  
633 New York, USA. pp. 249–256. doi:[10.1145/218380.218448](https://doi.org/10.1145/218380.218448).
- 634 Sweby, P.K., 1984. High resolution schemes using flux limiters for hyperbolic  
635 conservation laws. *SIAM Journal of Numerical Analysis* 21, 995–1011.
- 636 Walker, I.J., 2000. Secondary airflow and sediment transport in the lee of  
637 transverse dunes. Ph.D. thesis. University of Guelph. Ottawa, Canada.
- 638 Walker, I.J., Nickling, W.G., 2002. Dynamics of secondary airflow and sediment  
639 transport over and in the lee of transverse dunes. *Prog. Phys. Geog.* 26, 47–75.  
640 doi:[10.1191/0309133302pp325ra](https://doi.org/10.1191/0309133302pp325ra).
- 641 Walker, I.J., Nickling, W.G., 2003. Simulation and measurement of surface  
642 shear stress over isolated and closely spaced transverse dunes in a wind tunnel.  
643 *Earth Surf. Proc. Land.* 28, 1111–1124. doi:[10.1002/esp.520](https://doi.org/10.1002/esp.520).